

# Exchange spin-orbit coupling and unconventional p-wave magnetism

Anna Birk Hellenes,<sup>1</sup> Tomáš Jungwirth,<sup>2,3</sup> Jairo Sinova,<sup>1,2</sup> and Libor Šmejkal<sup>1,2</sup>

<sup>1</sup>*Institut für Physik, Johannes Gutenberg Universität Mainz, D-55099 Mainz, Germany*

<sup>2</sup>*Institute of Physics, Czech Academy of Sciences, Cukrovarnická 10, 162 00, Praha 6, Czech Republic*

<sup>3</sup>*School of Physics and Astronomy, University of Nottingham, NG7 2RD, Nottingham, United Kingdom*

(Dated: September 6, 2023)

Spin-orbit coupling arising from the relativistic Dirac equation underpins fundamental and applied research areas such as the spin Hall effects and topological insulators. This Dirac mechanism of spin-orbit coupling induces in non-centrosymmetric crystals a momentum-dependent spin splitting typically limited to a meV scale unless involving heavy and often toxic elements. Here we identify a previously overlooked mechanism that shares with the Dirac mechanism the characteristic signature of spin-orbit coupling, namely the antisymmetric time-reversal-invariant spin polarization in the band structure. In contrast to the relativistic Dirac equation, our spin-orbit coupling arises from the magnetic exchange interaction in non-centrosymmetric crystals with a non-coplanar spin order. An unconventional p-wave magnetic phase, corresponding to this exchange spin-orbit coupling, represents a long-sought but elusive realization of a magnetic counterpart of the p-wave phase of superfluid He-3. We identify type-A exchange spin-orbit coupling realized on mutually-shifted opposite-spin Fermi surfaces, and type-B on one Fermi surface. We predict giant spin splitting magnitudes on the scale of hundreds of meV in realistic material candidates, namely in antiperovskite  $\text{Ce}_3\text{InN}$  and  $\text{Mn}_3\text{GaN}$ . Our results open a possibility for realizing large exchange spin-orbit coupling phenomena in materials comprising abundant light elements and with implications in fields ranging from spintronics, dissipationless nanoelectronics and quantum electronics, to topological matter.

## INTRODUCTION

Spin-orbit coupling can arise in the  $1/c^2$  ( $c$  is the speed of light) expansion around the non-relativistic limit of the Dirac equation, taking the form of an internal effective field acting on the electron spin [1]. This Dirac spin-orbit-coupling mechanism can thus be viewed as a single-quasi-particle effect, leading to numerous phenomena of fundamental and applied interest in areas including the anomalous and spin Hall effects [2–4], magnetic anisotropy, charge-spin conversion, topological insulators, or quantum computing [5–7]. In the momentum space of the electronic structure of non-centrosymmetric crystals, the Dirac spin-orbit coupling leads to an antisymmetric spin splitting with linear band-dispersion around the  $\Gamma$ -point, that does not break time-reversal ( $\mathcal{T}$ ) symmetry [6]. The magnitude of the Dirac spin-orbit coupling scales with a power of the atomic number [8]. It is thus sizable only in crystals with heavy and often toxic elements. Here, the record values of  $\sim 100$  meV are reached, e.g., in BiTeI [9].

A realization of alternative mechanisms of spin-orbit coupling that would not require the strongly relativistic heavy elements has remained for decades one of the outstanding open problems in condensed-matter physics [10, 11]. Particularly appealing candidates are mechanisms based on the strong Coulomb interaction operating directly in the non-relativistic limit of the Dirac equation without relying on the perturbatively weak  $1/c^2$  expansion. In magnetically-ordered systems, the Coulomb-exchange interaction was envisaged to enable such a mechanism [10, 11], which we will refer to as exchange spin-orbit coupling. As perceived, it

would share with the above Dirac spin-orbit coupling the antisymmetric spin polarization and  $\mathcal{T}$ -symmetry in the electronic structure, but its strength could be potentially orders of magnitude larger and would not rely on the presence of the relativistic heavy elements. However, a real physical realization of the corresponding unconventional p-wave magnetic phase has been elusive. Moreover, in the context of Fermi-liquid instabilities in strongly correlated magnets, general principle obstacles have been identified that could prohibit the formation of a correlated p-wave magnetic phase [12, 13].

In contrast, even-parity-wave (d, g, or i-wave) collinear magnetism has been recently predicted and classified in a range of materials by a spin-group formalism [14, 15]. This symmetry formalism is designed to describe magnetism in the non-relativistic limit of the Dirac equation [14, 15]. Unlike the conventional relativistic magnetic groups tailored to the description of the full Dirac equation, the symmetry transformations in the non-relativistic spin groups consider pairs of generally different operations,  $[R_i||R_j]$ , acting in uncoupled spin space (left of the double vertical bar) and real space (right of the double vertical bar). The spin-group classification enabled to identify the even-parity-wave collinear magnetism, the so-called altermagnetism, in materials ranging from insulators to superconductors, and to demonstrate their unconventional phenomenology, particularly in the field of spintronics [14–25].

The principally distinctive feature of altermagnets, in comparison to the envisaged exchange spin-orbit coupling of the p-wave magnets, is the symmetric alternation of the spin polarization and broken  $\mathcal{T}$ -symmetry in the electronic structure. This distinction between (d-wave)

altermagnets and p-wave magnets is illustrated in Fig. 1.

We note that the symmetric spin polarization and broken  $\mathcal{T}$ -symmetry in the electronic band structure can be also identified in certain non-collinear magnetic orderings [4, 26, 27], as recalled in Fig. 1. However, unlike the collinear altermagnets with a common momentum-independent spin-quantization axis, the symmetric spin polarization in the band structure of non-collinear magnets appears when choosing a particular spin projection. The magnitude of this spin projection then tends to vary across the momentum space (see Fig. 1 and Fig. S1). Analogous symmetric spin polarizations were also predicted to arise in strongly correlated systems [28].

The above-described realization of the symmetric spin polarization in the d-wave (or higher even-parity wave) altermagnets prompts a question of whether the exchange spin-orbit coupling, with the characteristic antisymmetric spin polarization of a p-wave magnet, can be identified in realistic material candidates starting from the spin-symmetry considerations of the magnetic crystal structure. In this manuscript, we affirmatively answer this question by demonstrating the exchange spin-orbit coupling that arises from a non-centrosymmetric non-coplanar magnetic order on an antiperovskite ( $\text{Ce}_3\text{InN}$  or  $\text{Mn}_3\text{GaN}$ ) crystal with a  $[\mathcal{T}||\mathcal{T}\tau]$  symmetry (here  $\tau$  is translation). In analogy to the classification of the superfluid He-3 phases [29–31], we identify two distinct types of the p-wave magnetism in these crystals: type-A with the exchange spin-orbit coupling realized on mutually-shifted (deformed) opposite-spin Fermi surfaces, and type-B realized on one (deformed) Fermi surface (see Fig. 1).

### SPIN-SYMMETRY CONDITIONS FOR EXCHANGE SPIN-ORBIT COUPLING AND P-WAVE MAGNETISM

In Fig. 1, we illustrate the spin symmetry criteria for the emergence of the exchange spin-orbit coupling and the unconventional p-wave magnetism. The antisymmetrically spin split  $\mathcal{T}$ -invariant energy bands are defined as

$$\epsilon(s, \mathbf{k}) = \epsilon(-s, -\mathbf{k}). \quad (1)$$

Here  $s$  refers to the spin and  $\mathbf{k}$  to the wavevector. Commonly, this spin splitting is achieved by the relativistic Dirac spin-orbit coupling in non-centrosymmetric crystals with  $\mathcal{T}$  or  $\mathcal{T}\tau$  symmetry in their relativistic magnetic group [32] (here  $\tau$  is translation).

To generate the exchange spin-orbit coupling, we need to fulfil counterpart symmetry conditions applicable for magnetically ordered crystals in the non-relativistic limit, which can be formulated within the non-relativistic spin-symmetry formalism [14]:

(i) The  $\mathcal{T}$ -invariance of the non-relativistic band structure is protected for all types of spin arrangements on crystals that obey a  $[\mathcal{T}||\mathcal{T}\tau]$  symmetry.

(ii) The antisymmetric spin polarization requires non-centrosymmetric crystals. In the spin-symmetry formalism, this is expressed as magnetic crystals breaking the  $[E||\mathcal{P}]$  symmetry. Here,  $\mathcal{P}$  is the real-space inversion, and  $E$  is the spin-space identity.

Consistent with the symmetry conditions (i) and (ii), we identify the exchange spin-orbit coupling and p-wave magnetism in non-centrosymmetric non-coplanar magnets with the non-relativistic  $[\mathcal{T}||\mathcal{T}\tau]$  spin symmetry (Fig. 1).

We note that these crystals belong to the type-IV relativistic magnetic groups characterized by the presence of the magnetic  $\mathcal{T}\tau$  symmetry. One of the reasons why the exchange spin-orbit coupling and p-wave magnetism has remained elusive prior to our work is the earlier expressed notion that a non-relativistic spin splitting is excluded in all magnets corresponding to the type-IV relativistic magnetic groups [33, 34]. The argument justifying this notion is based on assuming that, besides the  $\mathcal{T}\tau$  symmetry, all magnets corresponding to the type-IV magnetic groups have the  $C_2\tau$  symmetry [33, 34]. Here,  $C_2$  is a  $180^\circ$  spin-space rotation around one common axis. However, the argument omits that the type-IV relativistic magnetic groups also include non-coplanar magnets and that these break the spin-space  $C_2\mathcal{T}$  symmetry (the spin-group  $[C_2\mathcal{T}||\mathcal{T}]$  symmetry).

Below we demonstrate the exchange spin-orbit coupling and p-wave magnetism in specific non-coplanar non-centrosymmetric crystals.

### P-WAVE TIGHT-BINDING MODEL

We first illustrate the exchange spin-orbit coupling on a tight-binding model of a type-B (spin channel) p-wave magnet shown in Fig. 2. The model comprises a kagome lattice with a non-coplanar magnetic ordering, which fulfils the above symmetry criteria for the p-wave magnetism. The non-coplanar magnetic order breaks the  $[C_2\mathcal{T}||\mathcal{T}]$  symmetry and, simultaneously, it preserves the  $[\mathcal{T}||\mathcal{T}\tau]$  symmetry, as shown in Fig. 2(a) by the magenta arrow. The magnetic order also removes the inversion centers of the kagome lattice, marked by the black crosses in Fig. 2(a). The inversion symmetry would require connecting the same spins. However, as highlighted by the dashed double arrow in Fig. 2(a), it connects opposite spins and thus breaks the inversion symmetry.

The corresponding model Hamiltonian reads,

$$H = \sum_i \mathbf{J} \cdot \boldsymbol{\sigma}_i^\dagger c_i + \sum_{\langle ij \rangle} t c_i^\dagger c_j. \quad (2)$$

Here, the first term is the local exchange field at each site

whose size and direction is parametrized by  $\mathbf{J}$ , and  $\boldsymbol{\sigma}$  is a vector containing the three spin Pauli matrices. The second term describes nearest-neighbor hoppings on the kagome lattice with the hopping amplitude  $t$ .

In reciprocal space, the first Brillouin zone is shown by the darker grey parallelogram in Fig. 2(b). The Brillouin zone is spanned by the reciprocal vectors  $\mathbf{b}_1 = (\pi, -\pi/\sqrt{3})$  and  $\mathbf{b}_2 = (0, 4\pi/\sqrt{3})$ . By comparison, the Brillouin zone for a hexagonal unit cell of the nonmagnetic kagome lattice is the larger dark/light grey parallelogram or the blue hexagon in Fig. 2(b).

We now demonstrate the exchange spin-orbit coupling and the type-B (spin-channel) p-wave magnetism in this model. We consider  $|\mathbf{J}| = t$  and carry out the calculations numerically using the PythTB package version 1.7.2 [35]. The p-wave spin polarization is illustrated on the Fermi surface for Fermi energy of  $0.65t$ .

This Fermi-surface spin polarization preserves the  $\mathcal{T}$  symmetry in momentum space at every wavevector, as seen in Fig. 2(c). We highlight the p-wave spin polarization by the red and blue color of the spin expectation values, with a component either along  $\langle S_x \rangle$  (blue) or  $-\langle S_x \rangle$  (red).

Every red-colored spin at a wavevector  $\mathbf{k}$  has a partner at the opposite wavevector,  $-\mathbf{k}$ , with opposite, blue-colored spin. This antisymmetric spin polarized electronic structure thus agrees with Eq. (1). Additionally, the spins wind once around the Fermi surface, akin to the relativistic Rashba spin-orbit coupling. However, unlike in the Rashba case, our exchange spin-orbit coupled states are not helically-locked, and both their phase and magnitude depend on the wavevector.

The spin polarized band structure for our model non-coplanar magnet is shown in Fig. 2(d). The bands also reflect the type-B (spin channel) p-wave phase and the  $\mathcal{T}$  symmetry. This is illustrated in Fig. 2(d) by comparing the spin polarized bands along the  $\Gamma M_2$  and  $-M_2\Gamma$  paths. For instance, the  $\langle S_x \rangle$  spin polarization, shown in the left panel of Fig. 2(d), has opposite signs along the opposite paths. The same holds for  $\langle S_y \rangle$ , while  $\langle S_z \rangle$  is zero in our model.

As a reference, we illustrate the absence of the exchange spin-orbit coupling and p-wave magnetism in our model kagome lattice when considering a collinear order, instead of the non-coplanar order. An example of the collinear magnetic configuration with the  $[\mathcal{T}||\mathcal{T}\boldsymbol{\tau}]$  symmetry is shown in Supplementary Fig. S2. The corresponding energy bands are spin degenerate across the whole Brillouin zone, as illustrated in Fig. 2(e).

## AB INITIO IDENTIFICATION OF ANTIPEROVSKITE P-WAVE MAGNETISM CANDIDATES

We now demonstrate, based on our symmetry analysis and *ab initio* calculations, realistic material candidates of the exchange spin-orbit coupling and type-A and type-B p-wave magnetism within the family of antiperovskite crystals. The cubic lattice of the nonmagnetic antiperovskite crystal structure contains five atoms. The experimentally reported non-coplanar magnetic state of antiperovskite  $\text{Ce}_3\text{InN}$  leads to a doubling of the unit cell as compared to the nonmagnetic phase, i.e., it has the required  $[\mathcal{T}||\mathcal{T}\boldsymbol{\tau}]$  spin symmetry (corresponding to a type-IV magnetic space group  $P_C42_12$  [36]).

Figure 3(a) shows the crystal and magnetic structure of  $\text{Ce}_3\text{InN}$  in the (201)-plane. Remarkably, in this plane, the non-coplanar magnetic moments form the double kagome structure analogous to our model in Fig. 2. For example, the first three Ce atoms in the top-left triangle are related to the last three atoms in the top-right triangle by the  $[\mathcal{T}||\mathcal{T}\boldsymbol{\tau}]$  spin symmetry with  $\boldsymbol{\tau} = (\frac{1}{2}, \frac{1}{2}, -1)$ . The grey-shaded box is the tetragonal unit cell. Figure 3(b) shows the unit cell in the (001)-plane. The unit cell contains ten atoms in total, as explicitly shown in the Supplementary Fig. S3.

To illustrate the non-relativistic exchange spin-orbit coupling in materials containing low atomic-number elements, we also consider a system with a magnetic sublattice of Ce (atomic number 58) substituted by Mn (atomic number 25) [37]. Except for the values of the lattice parameters, the lattice structures of  $\text{Mn}_3\text{GaN}$  and  $\text{Ce}_3\text{InN}$  are identical [38]. The Mn, Ga, and N sites are shown in the legend in Fig. 3(a). The corresponding Brillouin zone for both materials is shown in Fig. 3(c).

We calculate the band structure using the Vienna Ab Initio Simulation Package (VASP), the Perdew-Burke-Ernzerhof (PBE) exchange-correlation functionals [39–41], constrained non-coplanar magnetism, symmetrization switched off, and in the non-relativistic limit (without relativistic spin-orbit coupling). We add a penalty potential to converge the non-coplanar magnetic calculations (see Methods for details).

Fig. 3(d) shows the resulting constant-energy surface cut of  $\text{Ce}_3\text{InN}$ . The cut lies in the (100)-plane ( $\mathbf{k}_x = 0$ ), which is indicated in blue in Fig. 3(c). The considered constant energy is 0.19 eV above the Fermi level obtained from the self-consistent *ab initio* calculation. The spin polarized constant-energy surfaces take the type-A p-wave form (cf. Fig. 1). They are  $\mathcal{T}$ -invariant and show the characteristic mutual shift of the (deformed) constant-energy surfaces with opposite spins, resulting in nodes in both spin and charge channels.

The type-B p-wave spin polarization is shown in Fig. 3(e) for  $\text{Mn}_3\text{InN}$  (cf. Fig. 1). The constant-energy surface cut for an energy 1.36 eV below the Fermi level

is in the (001)-plane indicated in dark grey in Fig. 3(c). There is a single spin polarized constant-energy surface, i.e., it is nodeless in the charge channel. The spin polarization is antisymmetric and preserves the  $\mathcal{T}$  symmetry.

Finally, we demonstrate the large scale of the spin splitting induced by the non-relativistic exchange spin-orbit coupling. In Figs. 4(a,b) we show the *ab initio* band structures of  $\text{Ce}_3\text{InN}$  and  $\text{Mn}_3\text{GaN}$ , respectively. The bands with spin projections are plotted along the  $X\Gamma - X$  and  $M\Gamma - M$  paths (for more band structures see Supplementary Figs. S4,5). We observe a giant magnitude of the spin splitting in both materials. In  $\text{Mn}_3\text{GaN}$ , the two bands that are well-separated from all the other bands have a spin splitting as large as  $\approx 260$  meV. We point out that deeper in the Fermi sea, where many bands overlap, we can track even larger spin splitting of  $\approx 800$  meV, as shown in Supplementary Fig. S6. Such a large spin splitting is at least 1-2 orders of magnitude stronger than the relativistic spin splitting induced by the Dirac spin-orbit coupling in the same material. For both materials, we also observe a linear band dispersion around the spin-degenerate  $\Gamma$ -point. This is another characteristic feature that our non-relativistic exchange spin-orbit coupling shares with the established relativistic Dirac mechanism.

## DISCUSSION AND SUMMARY

In our work, we have identified the analogy of superfluid He-3 in unconventional higher parity-wave magnetism, that has been elusive for many decades [10, 11]. While in our unconventional p-wave magnetism, we consider ordering of electrons in the spin (and charge) channel, in superfluidity [29] the ordering corresponds to the p-wave Cooper pairing of the fermionic He-3 atoms [30]. The superfluid He-3 is known to host a plethora of rich and anisotropic properties and, thus, similarly intriguing physics can now start to emerge in magnets, following our identification of first realistic material candidates of the p-wave phase. Unconventional spin currents are an example of extraordinary phenomena that have been anticipated in the p-wave magnets [11].

Our results break with the earlier expressed notion [33, 34, 42] that it is impossible to realize a non-relativistic spin splitting in compensated magnets with opposite spin channels related by lattice translation, i.e., in magnets corresponding to the type-IV relativistic magnetic space groups.

We point out that our unconventional p-wave magnetism is principally different from the multipolar [43] and non-coplanar orderings [44–46] studied in magnetic crystals that do not exhibit the non-relativistic  $[\mathcal{T}||\mathcal{T}\tau]$  spin symmetry (do not correspond to the type-IV relativistic magnetic space groups). Our identification

of p-wave magnetism, based on specific non-relativistic spin symmetries of crystals with a non-coplanar magnetic order, is also conceptually different from, the so far unsuccessful, attempts to realize p-wave magnetism via strongly correlated instabilities and hidden orders [47]. Our p-wave magnetism can materialize already on a single quasiparticle level of density functional theory, and thus opens the possibility of its robust realization and observation in both metallic and insulating magnets.

Our exchange spin-orbit coupling is a strong non-relativistic mechanism for generating antisymmetric spin polarization in the electronic structure, making it a favorable alternative of the conventional and comparatively weaker Dirac spin-orbit coupling. We have demonstrated that the exchange mechanism can lead to large spin splittings reaching an eV magnitude, which is unparalleled for the relativistic spin-orbit coupling. The linear dispersion around the  $\Gamma$ -point is also a promising feature to be explored in the context of topological spintronics and Weyl-fermion physics [48, 49].

Our identification of the p-wave magnetism and exchange spin-orbit coupling in realistic material candidates thus opens a broad range of research directions in both fundamental and more applied fields. On a fundamental level, the non-coplanar p-wave magnets complement the conventional ferromagnets with the principally s-wave type of order, the conventional antiferromagnets [14, 50] with no spin polarization order in the electronic structure, as well as the recently discovered collinear altermagnets with the d-wave (or higher even-parity wave) order [14, 15]. From a practical perspective, the exchange spin-orbit coupling in our p-wave magnets opens the possibility for realizing strong spintronic phenomena and functionalities in areas that in the past have been governed by the perturbatively-weak relativistic spin-orbit coupling and required the inclusion of heavy elements. The fundamental and applied research fields that can potentially benefit from our unconventional form of magnetism and spin-orbit coupling, generating a robust p-wave spin-momentum locking and large Fermi surface anisotropies, thus include anomalous and spin Hall effects, topological insulators, or charge-spin conversion phenomena and functionalities in spintronic devices.

## ACKNOWLEDGMENTS

We acknowledge fruitful discussions with Jörg Schmalian, Rafael M. Fernandes, and Andrey Chubukov. We acknowledge funding from the Czech Science Foundation Grant No. 19-18623X, the Ministry of Education of the Czech Republic Grants No. LM2018096, LM2018110, LM2018140, and LNSM-LNSpin, Deutsche Forschungsgemeinschaft Grant TRR 173 268565370 (project A03) and TRR 288 42221347

(project B05), the Johannes Gutenberg University Grant TopDyn, the computing time granted on the supercomputer Mogon at Johannes Gutenberg University Mainz (hpc.uni-mainz.de), and the support of Alexander Von Humboldt Foundation.

## METHODS

**Density functional theory.** For both materials, we constrained the magnetic moment direction and size. The constraining procedure introduces an energy penalty if the magnetic moments deviate from the constraining magnetic moment [51]. For  $\text{Ce}_3\text{InN}$ , we used an initial magnetic moment size of  $3.5 \mu_B$  on each magnetic site, a constraining magnetic moment size of  $1.0943 \mu_B$ , an energy weight factor  $\lambda = 2 \text{ eV}$ , and radii of  $1.198 \text{ \AA}$  for Ce and N, and  $1.694 \text{ \AA}$  for In, within which the local magnetic moments are integrated. For  $\text{Mn}_3\text{GaN}$ , the initial magnetic moment size we used was  $3.5 \mu_B$ , the constraining magnetic moment size was  $2 \mu_B$ ,  $\lambda = 3 \text{ eV}$ , and the radii within which the magnetic moments are integrated were  $0.922911 \text{ \AA}$  for Mn and N, and  $1.30519 \text{ \AA}$  for Ga.

For  $\text{Ce}_3\text{InN}$ , we set the energy cut-off to  $600 \text{ eV}$  and included 176 bands for all calculations. The lattice parameters of the ten atom unit cell are  $a = b = 7.13421 \text{ \AA}$  and  $c = 5.04460 \text{ \AA}$ , corresponding to experimentally obtained lattice parameters [36, 52, 53]. For the energy bands, we used a  $4 \times 4 \times 7$  k-grid for the self-consistency calculation and the energy convergence criterion of  $5 \times 10^{-8} \text{ eV}$  for both the self-consistency and the band calculations. For the Fermi surface, we used a  $9 \times 9 \times 13$  k-grid for the self-consistency calculation, used the same energy convergence criterion, and used a  $31 \times 31$  k-grid for the (100) Fermi surface plane.

For  $\text{Mn}_3\text{GaN}$ , the energy cut-off was  $600 \text{ eV}$ , and we included 136 bands and used a convergence criterion of  $5 \times 10^{-6} \text{ eV}$  for all calculations. The lattice parameters are  $a = b = 5.49555 \text{ \AA}$  and  $c = 3.88594 \text{ \AA}$ , corresponding to experimentally measured lattice parameters [38]. We used a  $4 \times 4 \times 7$  k-grid for the self-consistency calculation for the bands. For the Fermi surface calculation, the k-grid was  $9 \times 9 \times 13$  for the self-consistency calculation and  $27 \times 27$  for the (001) Fermi surface plane.

We plotted the spin polarized Fermi surfaces using PyProcar version 5.6.6 [35].

and T. Jungwirth, *Reviews of Modern Physics* **87**, 1213 (2015).

- 
- [1] P. Strange, *Relativistic Quantum Mechanics*, 1st ed. (Cambridge University Press, Cambridge, 1998) p. 612.
- [2] N. Nagaosa, J. Sinova, S. Onoda, A. H. MacDonald, and N. P. Ong, *Reviews of Modern Physics* **82**, 1539 (2010), arXiv:0904.4154.
- [3] J. Sinova, S. O. Valenzuela, J. Wunderlich, C. Back,
- [4] L. Šmejkal, A. H. MacDonald, J. Sinova, S. Nakatsuji, and T. Jungwirth, *Nature Reviews Materials* **7**, 482 (2022), arXiv:2107.03321.
- [5] A. Manchon, H. C. Koo, J. Nitta, S. M. Frolov, and R. A. Duine, *Nature Materials* **14**, 871 (2015), arXiv:1507.02408.
- [6] A. Manchon, J. Železný, I. M. Miron, T. Jungwirth, J. Sinova, A. Thiaville, K. Garello, and P. Gambardella, *Reviews of Modern Physics* **91**, 035004 (2019), arXiv:1801.09636.
- [7] Y. Tokura, M. Kawasaki, and N. Nagaosa, *Nature Physics* **13**, 1056 (2017).
- [8] K. V. Shanavas, Z. S. Popović, and S. Satpathy, *Physical Review B* **90**, 165108 (2014).
- [9] K. Ishizaka, M. S. Bahrany, H. Murakawa, M. Sakano, T. Shimojima, T. Sonobe, K. Koizumi, S. Shin, H. Miyahara, A. Kimura, K. Miyamoto, T. Okuda, H. Namatame, M. Taniguchi, R. Arita, N. Nagaosa, K. Kobayashi, Y. Murakami, R. Kumai, Y. Kaneko, Y. Onose, and Y. Tokura, *Nature Materials* **10**, 521 (2011).
- [10] J. E. Hirsch, *Physical Review B* **41**, 6820 (1990).
- [11] C. Wu and S.-C. Zhang, *Phys. Rev. Lett.* **93**, 036403 (2004).
- [12] E. I. Kiselev, M. S. Scheurer, P. Wölfle, and J. Schmalian, *Physical Review B* **95**, 125122 (2017), arXiv:1611.01442.
- [13] Y.-M. Wu, A. Klein, and A. V. Chubukov, *Physical Review B* **97**, 165101 (2018), arXiv:1801.06571.
- [14] L. Šmejkal, J. Sinova, and T. Jungwirth, *Physical Review X* **12**, 031042 (2022).
- [15] L. Šmejkal, J. Sinova, and T. Jungwirth, *Physical Review X* **12**, 040501 (2022), arXiv:2204.10844.
- [16] L. Šmejkal, A. B. Hellenes, R. González-Hernández, J. Sinova, and T. Jungwirth, *Physical Review X* **12**, 011028 (2022), arXiv:2103.12664.
- [17] L. Šmejkal, R. González-Hernández, T. Jungwirth, and J. Sinova, *Science Advances* **6**, eaaz8809 (2020), arXiv:1901.00445.
- [18] I. I. Mazin, K. Koepf, M. D. Johannes, R. González-Hernández, and L. Šmejkal, *PNAS* **118**, e2108924118 (2021), arXiv:2105.06356.
- [19] Z. Feng, X. Zhou, L. Šmejkal, L. Wu, Z. Zhu, H. Guo, R. González-Hernández, X. Wang, H. Yan, P. Qin, X. Zhang, H. Wu, H. Chen, Z. Meng, L. Liu, Z. Xia, J. Sinova, T. Jungwirth, and Z. Liu, *Nature Electronics* **5**, 735 (2022).
- [20] R. González-Hernández, L. Šmejkal, K. Výborný, Y. Yahagi, J. Sinova, T. Jungwirth, and J. Železný, *Physical Review Letters* **126**, 127701 (2021), arXiv:2002.07073.
- [21] R. D. Gonzalez Betancourt, J. Zubáč, R. Gonzalez-Hernandez, K. Geishendorf, Z. Šobáň, G. Springholz, K. Olejník, L. Šmejkal, J. Sinova, T. Jungwirth, S. T. B. Goennenwein, A. Thomas, H. Reichlová, J. Železný, and D. Kriegner, *Physical Review Letters* **130**, 036702 (2023), arXiv:2112.06805.
- [22] A. Bose, N. J. Schreiber, R. Jain, D.-f. Shao, H. P. Nair, J. Sun, X. S. Zhang, D. A. Muller, E. Y. Tsymbal, D. G. Schlom, and D. C. Ralph, *Nature Electronics* **5**, 263 (2022), arXiv:2108.09150.
- [23] H. Bai, L. Han, X. Y. Feng, Y. J. Zhou, R. X. Su,

- Q. Wang, L. Y. Liao, W. X. Zhu, X. Z. Chen, F. Pan, X. L. Fan, and C. Song, *Physical Review Letters* **128**, 197202 (2022), arXiv:2109.05933.
- [24] S. Karube, T. Tanaka, D. Sugawara, N. Kadoguchi, M. Kohda, and J. Nitta, *Physical Review Letters* **129**, 137201 (2022), arXiv:2111.07487.
- [25] I. I. Mazin, *Physical Review B* **107**, L100418 (2023), arXiv:2301.08573.
- [26] J. Železný, Y. Zhang, C. Felser, and B. Yan, *Physical Review Letters* **119**, 187204 (2017), arXiv:1702.00295.
- [27] G. Gurung, D. F. Shao, and E. Y. Tsymbal, *Physical Review Materials* **5**, 124411 (2021).
- [28] L. Classen, A. V. Chubukov, C. Honerkamp, and M. M. Scherer, *Physical Review B* **102**, 125141 (2020).
- [29] A. J. Leggett, *Reviews of Modern Physics* **47**, 331 (1975).
- [30] D. Vollhardt and P. Woelfle, *The Superfluid Phases Of Helium 3*, reprint ed ed. (CRC Press, 2003) p. 656.
- [31] A. J. Leggett, (2003).
- [32] K. Yamauchi, P. Barone, and S. Picozzi, *Physical Review B* **100**, 245115 (2019).
- [33] S. A. Egorov, D. B. Litvin, and R. A. Evarestov, *The Journal of Physical Chemistry C*, acs.jpcc.1c02653 (2021).
- [34] Y. Guo, H. Liu, O. Janson, I. C. Fulga, J. van den Brink, and J. I. Facio, *Materials Today Physics* **32**, 100991 (2023), arXiv:2207.07592.
- [35] D. Vanderbilt, in *Berry Phases in Electronic Structure Theory* (Cambridge University Press, 2018) Chap. Appendix D, pp. 327–362.
- [36] F. Gäbler, W. Schnelle, A. Senyshyn, and R. Niewa, *Solid State Sciences* **10**, 1910 (2008).
- [37] H. K. Singh, I. Samathrakris, N. M. Fortunato, J. Zemen, C. Shen, O. Gutfleisch, and H. Zhang, *npj Computational Materials* **7**, 98 (2021), arXiv:2009.06440.
- [38] K. Shi, Y. Sun, J. Yan, S. Deng, L. Wang, H. Wu, P. Hu, H. Lu, M. I. Malik, Q. Huang, and C. Wang, *Advanced Materials* **28**, 3761 (2016).
- [39] G. Kresse and D. Joubert, *Physical Review B* **59**, 1758 (1999).
- [40] P. E. Blöchl, *Physical Review B* **50**, 17953 (1994), arXiv:arXiv:1408.4701v2.
- [41] J. P. Perdew, K. Burke, and M. Ernzerhof, *Physical Review Letters* **78**, 1396 (1996), arXiv:0927-0256(96)00008 [10.1016].
- [42] L.-D. Yuan, Z. Wang, J.-W. Luo, and A. Zunger, *Physical Review Materials* **5**, 014409 (2021).
- [43] S. Hayami, Y. Yanagi, and H. Kusunose, *Physical Review B* **101**, 220403 (2020), arXiv:2001.05630.
- [44] R. Shindou and N. Nagaosa, *Physical Review Letters* **87**, 116801 (2001), arXiv:0108322 [cond-mat].
- [45] Y.-P. Zhu, X. Chen, X.-R. Liu, P. Liu, H. Zha, C. Hong, J. Li, Z. Jiang, X.-M. Ma, Y.-J. Hao, W. Liu, M. Zeng, J. Ding, S. Mo, Z. Liu, M. Ye, D. Shen, R.-H. He, S. Qiao, Q. Liu, and C. Liu, (2023), arXiv:2303.04549.
- [46] W. Feng, J.-P. Hanke, X. Zhou, G.-Y. Guo, S. Blügel, Y. Mokrousov, and Y. Yao, *Nature Communications* **11**, 118 (2020), arXiv:1811.05803.
- [47] W. Knafo, S. Araki, G. Lapertot, D. Aoki, G. Knebel, and D. Braithwaite, *Nature Physics* **16**, 942 (2020).
- [48] L. Šmejkal, Y. Mokrousov, B. Yan, and A. H. MacDonald, *Nature Physics* **14**, 242 (2018), arXiv:1706.00670.
- [49] B. A. Bernevig, C. Felser, and H. Beidenkopf, *Nature* **603**, 41 (2022).
- [50] L. Šmejkal, J. Železný, J. Sinova, and T. Jungwirth, *Physical Review Letters* **118**, 106402 (2017), arXiv:1610.08107.
- [51] “I\_CONSTRAINED\_M - Vaspwiki,” [https://www.vasp.at/wiki/index.php/I\\_{\\_}CONSTRAINED\\_{\\_}M](https://www.vasp.at/wiki/index.php/I_{_}CONSTRAINED_{_}M), accessed: 2023-08-22.
- [52] S. V. Gallego, J. Manuel Perez-Mato, L. Elcoro, E. S. Tasci, R. M. Hanson, K. Momma, M. I. Aroyo, and G. Madariaga, *J. Appl. Cryst* **49**, 1750 (2016).
- [53] “Magndata - collection of magnetic structures,” [http://webbdcristal1.ehu.es/magndata/index.php?this\\_label=1.152](http://webbdcristal1.ehu.es/magndata/index.php?this_label=1.152), accessed: 2023-08-15.

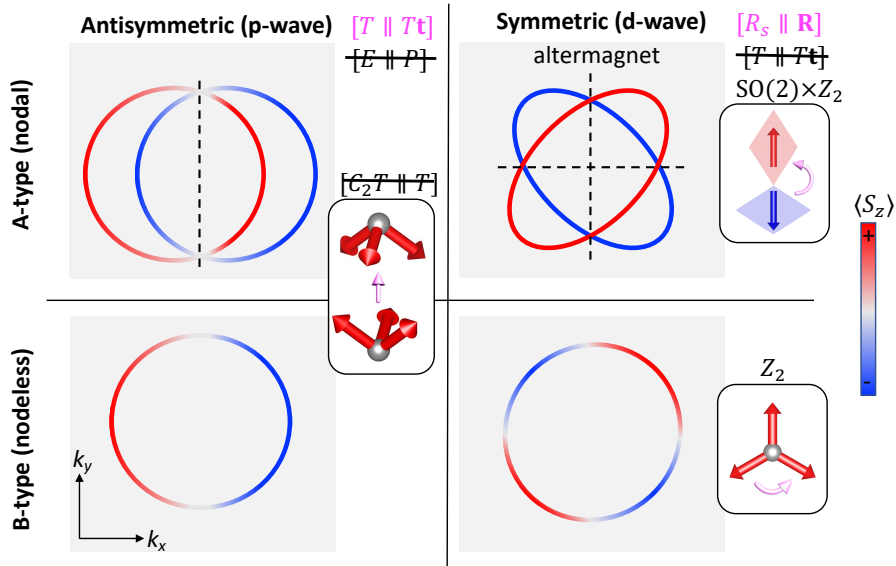


FIG. 1. Classification of spin polarized unconventional magnets with zero net magnetization. The spin polarization in reciprocal space, projected on the  $k_x - k_y$  plane, is shown in the four grey panels and emerges in collinear and non-collinear spin groups indicated in the insets. The first row shows type-A magnets with nodal planes in the spin channel and in the charge channel, highlighted by the dashed lines. The second row shows type-B magnets with nodal planes in the spin channel and without nodal planes in the charge channel. The left column shows antisymmetric spin polarizations, where the spin changes sign with inversion of the wavevector. The right column shows symmetric spin polarizations, where the spin remains invariant under wavevector-inversion. The antisymmetric spin polarizations shown here are of the p-wave type, which refers to the existence of a single nodal plane in the spin channel. The symmetric spin polarizations shown here are of the d-wave type, with two nodal planes in the spin channel.  $R_s$  and  $R$  denote rotation transformations in the spin and real space, respectively.  $SO(2)$  is a spin-only group in collinear magnets of spin rotations around the common spin axis.  $Z_2$  is a spin-only group containing, apart from identity, the spin-space transformation  $C_2\mathcal{T}$ .

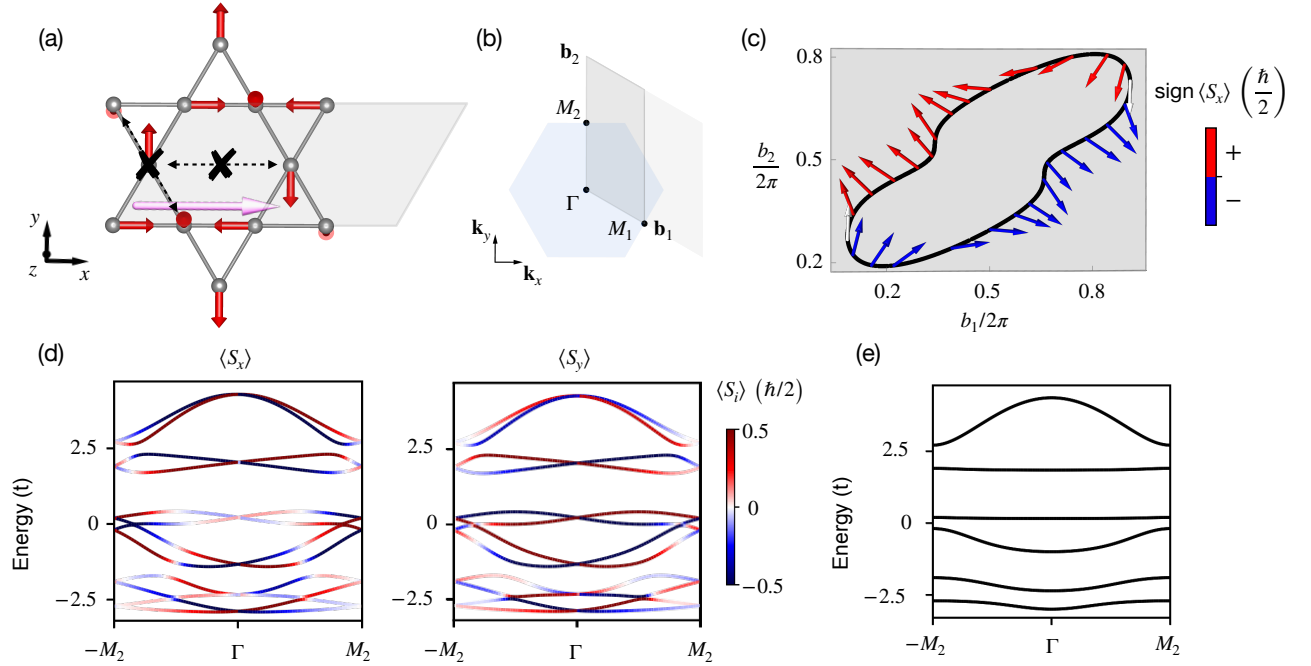


FIG. 2. Double unit cell kagome model. (a) Non-coplanar magnetic ordering in the model. The red arrows are the local spins at each site, and the gray parallelogram is the unit cell with  $\mathbf{a}_1 = (2, 0)$  and  $\mathbf{a}_2 = (1/2, \sqrt{3}/2)$ . The light pink arrow indicates the  $[\mathcal{T}||\mathcal{T}\tau]$  spin symmetry. The crosses show the inversion symmetry-breaking. (b) Brillouin zone spanned by the reciprocal vectors  $\mathbf{b}_1$  and  $\mathbf{b}_2$  (darker grey parallelogram), compared to the Brillouin zone of a single unit cell kagome crystal, or a hexagonal lattice (dark/light grey parallelogram or blue hexagon). The  $M_1$  and  $M_2$  points coincide with the  $M$ -points of the Brillouin zone of the hexagonal lattice. (c) Fermi surface of the model in (a) for  $|\mathbf{J}| = t$  and the Fermi energy of  $0.65t$ . The Fermi surface (black line) is shown as a function of  $b_1$  and  $b_2$  which are components of the wavevector along  $\mathbf{b}_1$  and  $\mathbf{b}_2$ , respectively. The arrows show the numerically calculated spin expectation values whose horizontal component is  $\langle S_x \rangle$  and vertical component is  $\langle S_y \rangle$ . The out-of-plane component,  $\langle S_z \rangle$ , is zero. The red and blue coloring highlights that the system has p-wave symmetry, where the spins are red for  $\langle S_x \rangle > 0$  and blue for  $\langle S_x \rangle < 0$ . (d) Band-structure along the  $-M_2\Gamma M_2$  path, colored by  $\langle S_x \rangle$  and  $\langle S_y \rangle$ . (e) Band-structure for a collinear magnetic configuration, also with  $|\mathbf{J}| = t$ , but where the three spins in top-left triangle in (a) point along  $z$ , and the three spins in the top-right triangle point along  $-z$  (see also Supplementary Fig. S2).

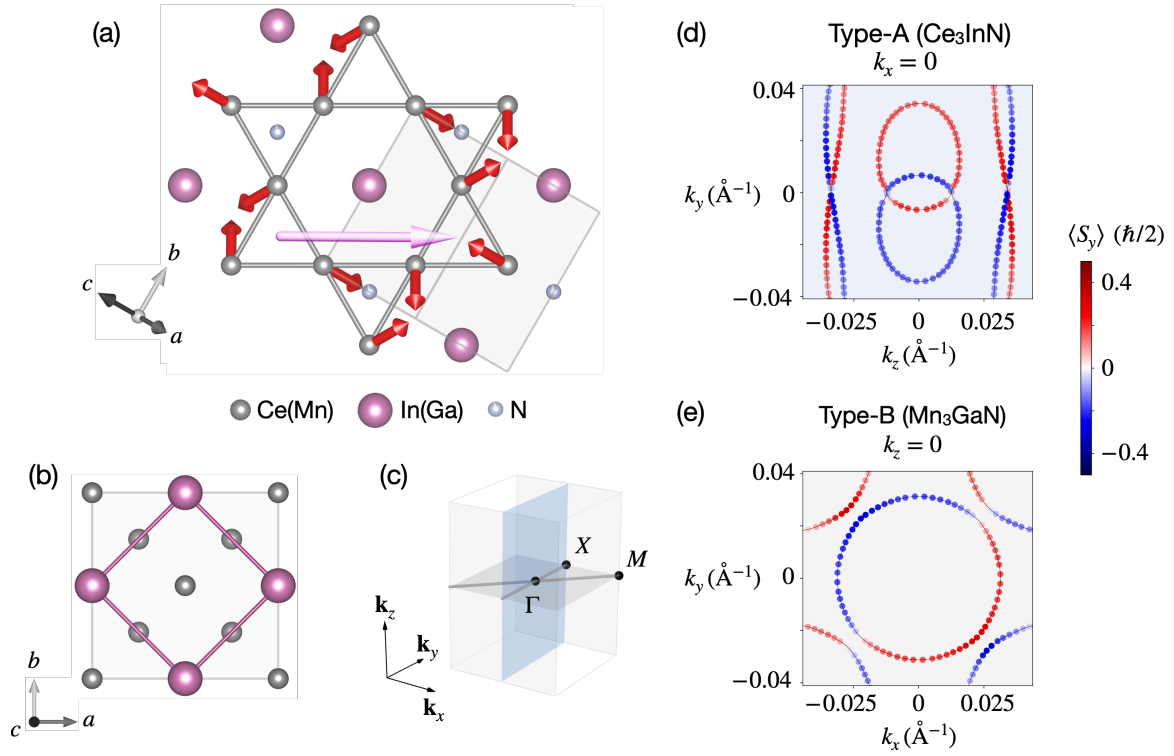


FIG. 3. Magnetic crystal structure and p-wave constant-energy surface cuts from *ab initio* calculations for  $\text{Ce}_3\text{InN}$  and  $\text{Mn}_3\text{GaN}$ . (a) The crystal structure of  $\text{Ce}_3\text{InN}$  and  $\text{Mn}_3\text{GaN}$  in the (201)-plane with magnetic moments indicated by red arrows. The crystal forms a kagome lattice with  $[\mathcal{T}||\mathcal{T}\tau]$  spin symmetry, where the translation  $\tau$  is shown by the light pink arrow. The gray sites are magnetic Ce (Mn), and the purple and light blue sites are In (Ga) and N, respectively. (b) The crystal projected on the (001)-plane. For ease of visualization, the magnetic-moment arrows are not shown. (c) First Brillouin zone for the tetragonal unit cell in (a,b). The blue and darker grey areas show the planes for which the Fermi surface cuts are calculated. The black points mark coordinates in the Brillouin zone. The grey thick lines mark paths in the Brillouin zone that join  $M$  and  $X$  with their inverse ( $-M$  and  $-X$ ). (d) The spin polarization along the  $\text{Ce}_3\text{InN}$  constant-energy surface cut in the blue (100)-plane in (c). The red and blue coloring indicates the in-plane  $\langle S_y \rangle$  spin polarization value. The energy for this constant-energy surface is 0.19 eV above the Fermi level. (e) The same as in (d), for  $\text{Mn}_3\text{GaN}$  in the (001)-plane (grey plane in (c)) for an energy 1.36 eV below the Fermi level.

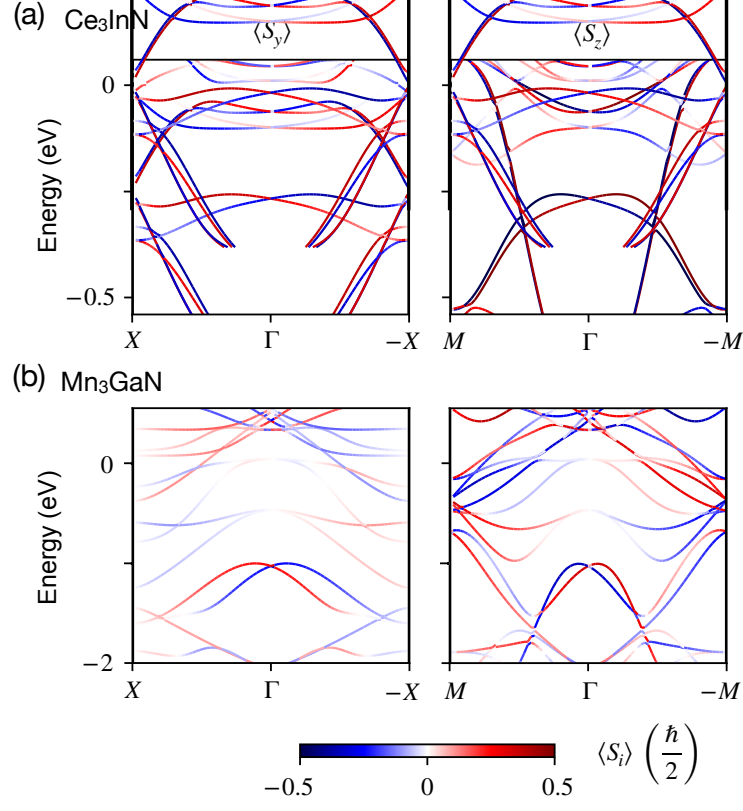


FIG. 4. *Ab initio* calculations showing spin split energy bands with  $\mathcal{T}$  symmetry and antisymmetric spin polarization. (a) Energy bands of Ce<sub>3</sub>InN. On the left are the bands along the  $X\Gamma-X$  path, see Fig. 3(c), colored by the spin polarization  $\langle S_y \rangle$ . On the right are bands along  $X\Gamma-X$  colored by  $\langle S_z \rangle$ . (b) The same for Mn<sub>3</sub>GaN. The spin splitting size is enhanced in Mn<sub>3</sub>GaN compared to Ce<sub>3</sub>InN. The other spin polarization components along these and additional paths are in the Supplementary Figs. S4 and S5.